Multipactor Suppression via Additive Manufacturing

Stephen V. Langellotti, *Member, IEEE*, Adam Brusstar, *Graduate Student Member, IEEE*,
Nicholas M. Jordan, *Senior Member, IEEE*, Y. Y. Lau, *Life Fellow, IEEE*,
and Ronald M. Gilgenbach, *Life Fellow, IEEE*

***Abstract*—Preventing multipactor is essential for ensuring vacuum electronic systems operate reliably. Textured materials have previously been shown to significantly reduce secondary electron emission. However, these surface treatments are difficult to achieve inside of coaxial structures. Additive manufacturing can be used to produce textured components that can suppress multipactor. The multipactor breakdown threshold in such coaxial transmission lines was experimentally measured using two different 3-D-printing technologies on two outer conductors. The partially 3-D-printed transmission line was found to dramatically reduce multipactor (up to 2.9 dB increase in threshold power); these experimental results consistently outperformed our prior particle-in-cell (PIC) simulations. This experimental study demonstrates proof-of-concept for using 3-D-printed materials to prevent multipactor.**

***Index Terms*—3-D-printing, coaxial transmission line, multipactor, particle-in-cell (PIC), secondary electron emission.**

I. INTRODUCTION

THE design of vacuum electronic systems requires specific care for preventing multipactor discharges. Multipactor is a form of plasma breakdown that occurs in vacuum systems when oscillating electric fields interact with free electrons [1], [2]. As the RF fields accelerate them into surfaces, the unbound electrons will multiply via secondary electron emission. This enables a rapidly growing electron cloud.

The ongoing electron bombardment against transmission line surfaces can lead to dangerous consequences. Multipactor

can cause cavity loading [3], [4] and potentially deteriorate signal quality [5]. As a worst-case scenario, multipactor may cause uncontrollable heat-up and catastrophic failure [6], [7]. In satellite communications systems, where repairing components is impossible, this is particularly dangerous.

Multipactor suppression is dependent on reducing secondary electron emission. There are two ways to do this. One way is to directly reduce the secondary emission yield (SEY) through material substitutions [8], [9], [10], [11] or surface treatments such as multipactor self-conditioning [9], [12], baking, and plasma cleaning [13], [14]; these methods remove surface impurities and reduce secondary electron emission, thus increasing breakdown voltages.

The second broad class of multipactor mitigation techniques attempts to indirectly alter the SEY. Instead of replacing the material properties, these methods manipulate the electron dynamics to make secondary electron emission less efficient. Disrupting the resonance between the electron motion and the oscillating electric field can reduce impact energies (and thus SEY). Many indirect methods have been explored; these include the introduction of external magnetic fields [15], [16], [17], [18], [19] or dc electric fields [9]. Other methods may include alterations to the RF waveform, such as through the use of modulated [20], [21] or nonsinusoidal [22] signals.

One final method for preventing multipactor is based on alterations to the surface topology [11], [23], [24], [25], [26], [27]. These methods focus on trapping the secondary electrons within the surface. Secondary electrons are emitted at some angle relative to the surface. If the material is perfectly smooth, nothing will prevent them from being ejected into the vacuum. This is not the case with a textured material; secondary electrons may impact against structures protruding from the surface. During these subsequent impacts, the secondary electrons may be reabsorbed, and this trapping effect will reduce the material's effective SEY.

This work evaluates the multipactor-suppression characteristics of two additive manufacturing technologies: selective laser melting (SLM) and atomic diffusion additive manufacturing (ADAM). These two processes represent differing extremes in 3-D printing. SLM is a powder-based technique where metallic powders are fused together using high-energy lasers [28]. On the other end of the spectrum, ADAM is based on the fused deposition modeling (FDM) method used in desktop 3-D printers; parts are printed using an adhesive-coated, metallic filament and then fired in a sintering oven [29].

These processes leave the material with an inherently textured surface. Components manufactured using SLM may
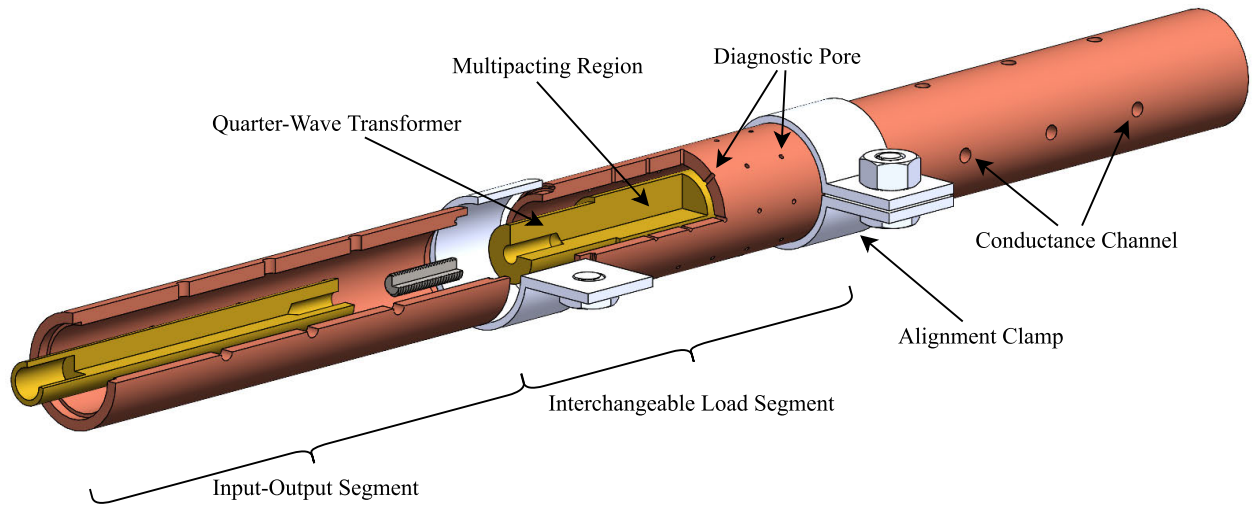
Fig. 1. Cutaway CAD rendering of the segmented, coaxial transmission line used in this experiment. An exploded view highlights the connection between the 50-Ω segments and the multipacting region.

have a "matte" surface finish [28], whereas ADAM-printed surfaces are dominated by the strata formed from the fusion of successive filament layers [29]. In our prior work [30], we used a ray-tracing, Monte-Carlo algorithm to generate modified SEY curves that account for the 3-D-printed surfaces' microscopic surface structures. This model predicted that the 3-D-printed materials will significantly reduce secondary emission, thus preventing multipactor; subsequent particle-in-cell (PIC) simulations showed significant improvements in the multipactor breakdown threshold. In this work, we present an experimental study to verify our simulations' results and demonstrate proof-of-concept of suppressing multipactor by the addition of 3-D-printed materials.

II. EXPERIMENTAL APPARATUS

This experiment uses the S-band (3.05 GHz) coaxial multipactor test cell facility at the University of Michigan [30], [31]. The coaxial transmission line has been modified from the design presented in [31]. It now includes an interchangeable load segment; a CAD rendering of the new design is shown in Fig. 1. Both the inner and outer conductors have been split into three distinct segments. At the input and output of the vacuum chamber are two 50-Ω characteristic impedance segments; these adapt to two MYAT 101-050 gas barriers which serve as RF windows separating the atmosphere from the vacuum. Base pressures are typically on the order of 0.25 μTorr (see the Appendix for estimates of the vacuum pressure within the transmission line). The central load segment contains the multipacting region. Here, the relatively small gap between the inner and outer conductors concentrates the multipactor discharge. An ultraviolet seed electron source is also present in this region. Not only does the seeding source encourage multipactor to occur, but it also increases the probability that the discharge will be initiated in this part of the transmission line. The narrow gap spacing in this portion of the transmission line also ensures that the peak electric fields are present here.

On the inner conductor, two quarter-wave transformers provide an impedance match across the length of the transmission line. A pair of directional couplers at the input and output of the vacuum chamber provide measurements of the
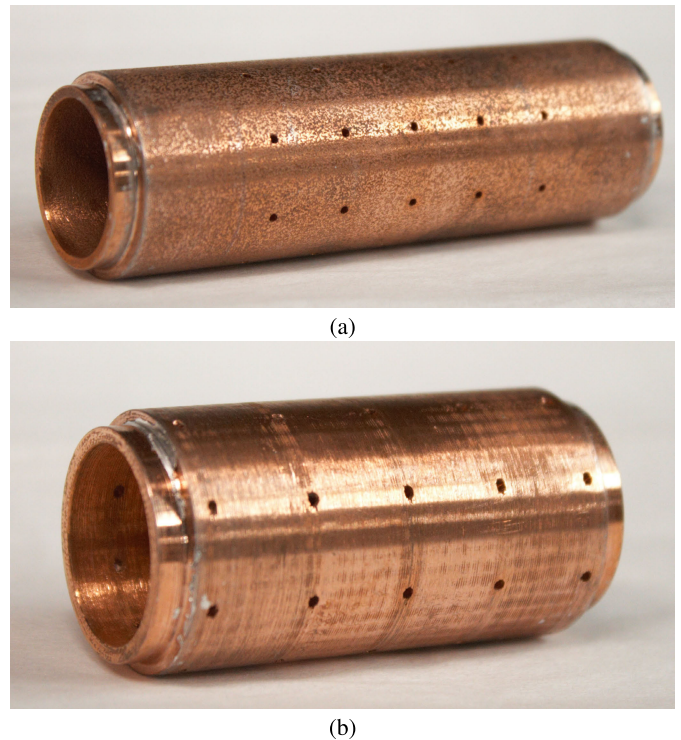
Fig. 2. Photographs of the two 3-D-printed outer conductors used in this experiment. (a) SLM-printed. (b) ADAM-printed. The SLM- and ADAM-printed segments are 76.2 and 50.8 mm long, respectively.

RF power that is supplied to, reflected by, and transmitted through the coaxial transmission line. Because we are using a fixed-frequency RF source, adjustments in *fd* are achieved by interchanging the inner conductor's central multipactor segment. This enables us to reduce the inner conductor's radius, thus altering the gap spacing *d*.

III. TRANSMISSION LINE FABRICATION

All transmission line components are manufactured from copper. The input–output segments and the inner conductors are each machined from OFHC copper; the outer

Fig. 3. SEM micrographs of the inner surfaces of the (a) SLM-printed, (b) ADAM-printed, and (c) machined outer conductors.

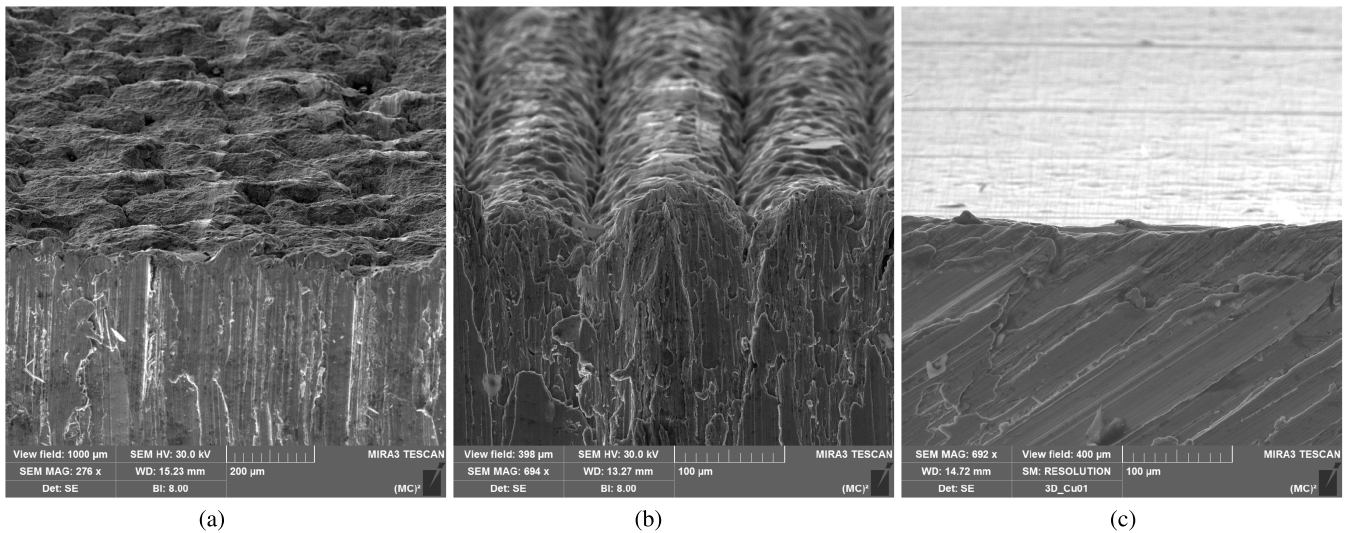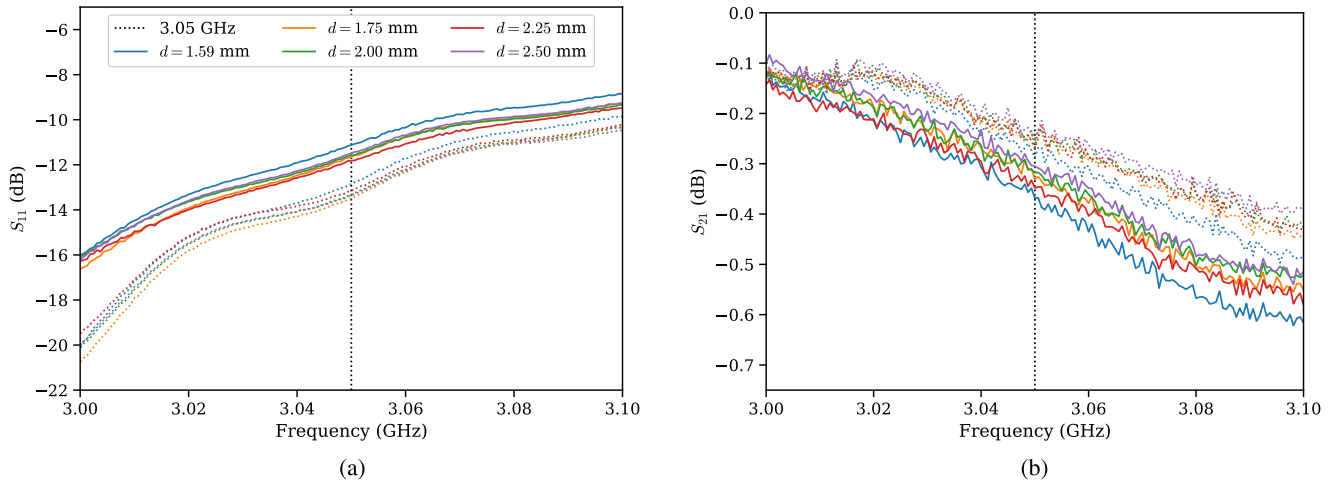Fig. 4. Cold test data (solid lines) of the coaxial transmission line with an SLM-printed outer conductor, with S_{11} in (a) and S_{21} in (b). These data are compared to data from the fully machined structures, which are shown as dotted lines. The vertical, dotted line represents the 3.05-GHz drive signal used in the experiment. (a) Reflected power, S_{11}. (b) Transmitted power, S_{21}.

conductor in the multipacting region was 3-D printed in copper using either SLM or ADAM. The SLM-printed outer conductor was manufactured from 15–53 μm copper powder with the following print settings: a laser power of 200 W, a scan speed of 300 mm s^{-1}, a hatch distance of 150 μm, and a layer thickness of 30 μm. The ADAM-printed outer conductor was produced using a Markforged MetalX printer with a postsintered layer height of 129 μm.

All tests performed using the SLM-printed and fully machined outer conductors used the same set of inner conductors. However, limitations from our third-party 3-D-printing service required us to shorten the ADAM-printed outer conductor segment. Likewise, the inner conductor's multipacting region (where the gap between the inner and outer conductors is smallest) was shortened to ensure that it is fully enveloped by the ADAM-printed outer conductor segment. Note that the UV seed electron source is only present in this region, thus increasing the probability that a discharge will only occur inside the multipactor region.

Photographs of the SLM [in Fig. 2(a)] and ADAM-printed [in Fig. 2(b)] outer conductor segments are shown in Fig. 2. In these photographs, the surface texture along the conductors' inner surfaces is readily apparent; the SLM-printed component features a matte surface finish, whereas the ADAM-printed segment is dominated by the layer line structures. Two SEM micrographs, performed by the Michigan Center for Materials Characterization, in Fig. 3 highlight these surface structures. The SLM-printed surfaces [in Fig. 3(a)] are dominated by an array of peaks and valleys; the ADAM-printed surfaces [in Fig. 3(b)] display long trench structures formed between successive filament layers. The significance of these microscale surface structures is further highlighted when we compare the 3-D-printed materials with the machined outer conductor, shown in Fig. 3(c).

The Michigan Center for Materials Characterization also performed an energy-dispersive X-ray spectroscopy (XEDS) analysis to confirm the material composition of the 3-D-printed outer conductors. Measurements were recorded at two locations within the conductor segments: at the conductors' inner

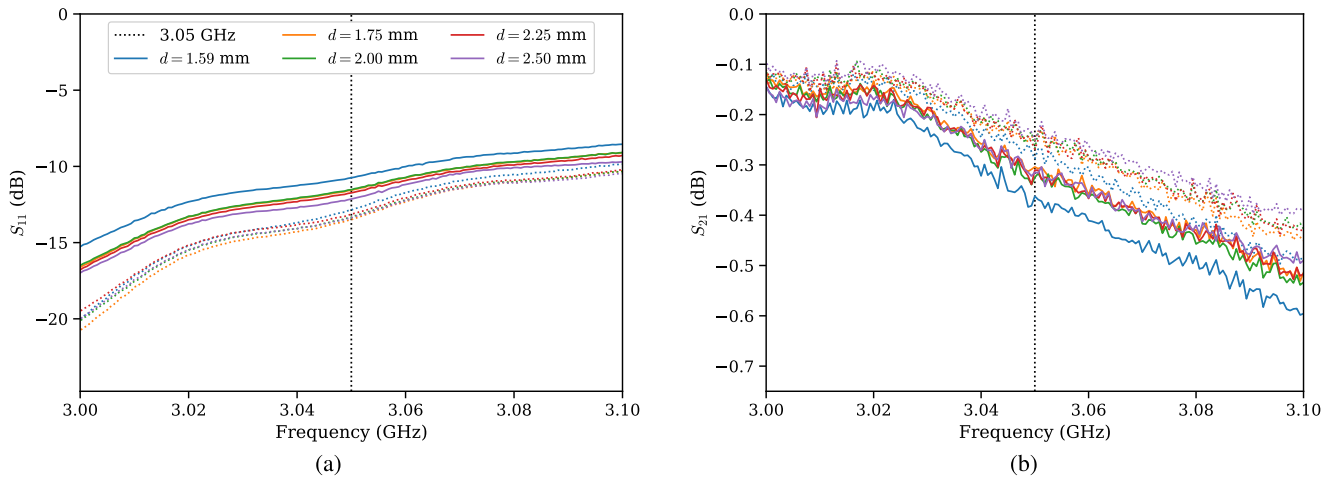(a)   (b)

Fig. 5.   Cold test data (solid lines) of the coaxial transmission line with an ADAM-printed outer conductor, with S_{11} in (a) and S_{21} in (b). Although high-power multipactor testing used a separate inner conductor, these cold tests were performed with the set of inner conductors that were used for both the machined and SLM-printed experiments to allow for better comparisons between the three configurations. The data for the fully machined surfaces are shown as dotted lines. The vertical, dotted line represents the 3.05 GHz drive signal used in the experiment. (a) Reflected power, S_{11}. (b) Transmitted power, S_{21}.

TABLE I
MATERIAL COMPOSITION OF THE 3-D-PRINTED SEGMENTS

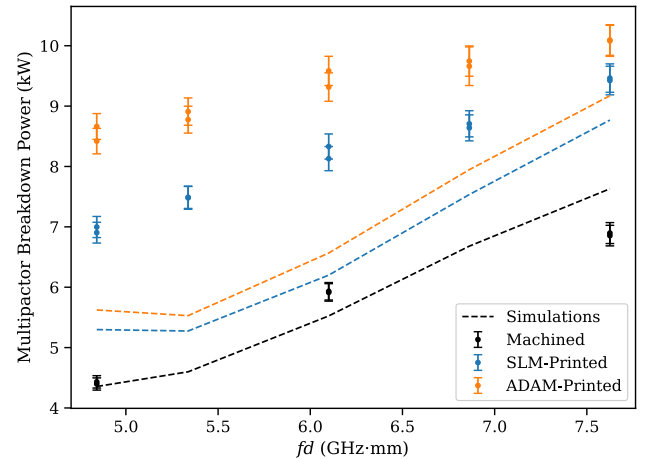| Element	Surface		Cross-Section	
	Weight %	Atom %	Weight %	Atom %
SLM-Printed				
Cu	85.22	63.22	92.55	84.69
O	9.25	27.24		
Al	3.61	6.31	4.49	9.67
Si	1.92	3.23	2.49	5.15
Fe			0.48	0.49
ADAM-Printed				
Cu	86.64	66.14	100	100
O	8.07	24.47		
Al	3.64	6.54		
Si	1.65	2.86		

Fig. 6.   Experimentally measured (solid lines) susceptibility diagram of a coaxial transmission line with a 3-D-printed outer conductor. Also shown are experimental data for the original machined surfaces (in black) and the PIC simulations of the printed transmission line (dashed lines).

surface inside the multipacting region, and at a cross-sectional cut along the conductors' lengths. These results are shown in Table I. The cross-sectional measurements reveal the 3-D-printed segments' bulk material composition: the ADAM-printed conductor is pure copper, and the SLM-printed segment has some aluminum, silicon, and iron impurities. At the conductors' inner surfaces, a large oxide layer is present. However, we speculate that these oxide layers are significantly reduced after multipactor self-conditioning [30], [31].

IV. EXPERIMENTAL RESULTS

A. Cold Testing

A series of cold tests were performed to ensure that the 3-D-printed transmission line did not significantly affect the signal quality. These results are shown in Figs. 4 and 5 for the SLM- and ADAM-printed cases, respectively. Recall that high-power multipactor tests are required using an alternative inner conductor with the ADAM-printed segment. To allow for better comparisons between all three configurations, all cold tests were performed with the same set of inner conductors.

In Figs. 4 and 5, dotted lines represent data from the original, fully machined transmission line. In both the SLM- and ADAM-printed cases, the transmission coefficient, S_{21}, only

shifted by approximately 0.1 dB. This is relatively insignificant and is on the same order of magnitude as our measurement uncertainties. The reflection coefficient, S_{11}, is affected somewhat more strongly. However, it is within an acceptable range. These data show that the 3-D-printed segments do not significantly perturb the transmission line's properties.

B. Multipactor Susceptibility

Experimental measurements of the multipactor susceptibility diagram were determined by finding the minimum RF power such that the reflected power signals were visibly perturbed by the multipactor discharge. These data are shown in Fig. 6. These measurements were performed after the transmission line had undergone a multipactor conditioning process, as described in [31]. Data corresponding to a fully machined transmission line is shown in black. Each experimental data point represents the average and standard deviation of five consecutive measurements. Between each experimental trial, the transmission line was briefly exposed
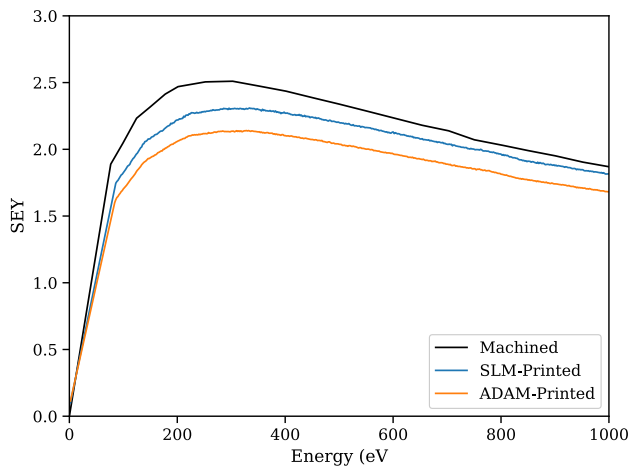
Fig. 7. SEY data for the 3-D-printed materials used in this experiment. Also shown are data for the machined surfaces, in black. These data were generated using the ray-tracing, Monte-Carlo algorithm described in [30].

to air and allowed to decondition. Also shown are data from PIC simulations (dashed lines) performed in CST Particle Studio. For the original, machined case, these simulations were performed using SEY data for nonbaked copper from Bojko et al. [13]. For the two 3-D-printed configurations, the SEY curves were modified using a Monte-Carlo, ray-tracing algorithm that simulates the electron trapping within the microscopic surface structures. The modified SEY curves are shown in Fig. 7. These simulations are described further in [30] and are based on previous work by Ye et al. [26]. Note that this model ignores any effects from the material impurities that are noted in Table I.

V. DISCUSSION AND CONCLUSION

Our experimental results show that the 3-D-printed transmission lines provided excellent resistance to multipactor. The SLM-printed outer conductor increased the breakdown threshold by 1.38–1.97 dB; this corresponds to a consistent increase of 2.5 kW. Even higher gains were achieved when using the ADAM-printed outer conductor (1.67–2.87 dB). These general trends agree with our PIC simulations. However, the increase in the breakdown threshold consistently surpassed the simulated predictions. This suggests that our modified SEY curves, which were based on an extreme simplification of the surface morphology, did not capture the full electron trapping effect [30]. Future PIC simulations could achieve higher levels of accuracy if we instead employed experimentally measured SEY curves for the 3-D-printed materials.

An interesting consequence of using these 3-D-printed materials arises when we consider that secondary emission from low-energy electrons tends to be due to backscattering and rediffusion. These processes are often treated as independent of the rest of the material's SEY properties: in the modified Vaughan model [32], we generally assume that the SEY is constant (typically 0.5–0.7) for all low-energy electrons. However, when we use our 3-D-printed materials, the SEY is lowered at all energies. This means that the efficiency of electron backscattering and rediffusion is significantly reduced. This could potentially eliminate ping-pong and other high-periodicity multipactor modes. During ping-pong modes, electrons will impact a single surface multiple times before

eventually crossing the gap [33], [34]. The single-surface impacts tend to occur at relatively low electron energies and thus require an efficient backscattering mechanism to ensure electrons are re-emitted so they can cross the gap. Since the textured surfaces disrupt low-energy secondary electron emission, ping-pong and other high-periodicity modes can be effectively shut down. This will severely reduce the parameter space that supports multipactor.

This work has shown that 3-D-printed transmission line structures may be able to significantly reduce the likelihood that a device will undergo multipactor. These components also did not significantly perturb the signals passing through the transmission line. This suggests that additive manufacturing could be used to produce drop-in replacements for existing components. Future work should further explore the limits of how 3-D printing affects multipactor discharges. In additive manufacturing, the surface topology can be extremely sensitive to the printer's settings. This property could be exploited to produce extremely porous materials that would efficiently trap electrons. However, these materials may distort a transmission line's electrical properties. This must be explored to ensure that the 3-D-printed components do not fundamentally alter the device's function. Dielectric materials, particularly plastics, are well suited to additive manufacturing. A future experiment could explore the multipactor characteristics of a 3-D-printed dielectric window. However, such a component may have issues with maintaining a vacuum seal.

APPENDIX
ESTIMATE OF VACUUM PRESSURE

Due to the nature of our coaxial transmission line, we cannot directly measure the pressure within the multipacting region. However, it can be estimated by considering the vacuum conductance between each transmission line region [35]. The multipactor region is vented through the two quarter-wave transformers that each have a conductance of C_{QWT}. The quarter-wave transformers are, in turn, vented through a series of 3.18-mm conductance channels (each with conductance C_{ch}) in the input–output segments (12 channels per segment). For simplicity, we assume that the vacuum pressure inside the input–output segments is uniform. Thus, the total conductance across each input–output segment is $C_{io} = 12C_{ch}$. The total vacuum conductance between the main vacuum chamber and the multipacting region is thus

$$C_{net} = 2\left[\frac{1}{C_{QWT}} + \frac{1}{C_{io}}\right]^{-1}. \tag{A.1}$$

Once we have obtained the transmission line's conductance, the pressure in the multipacting region is simply

$$P_{mp} = P_0 + \frac{Q}{C_{net}} \tag{A.2}$$

where P_0 is the pressure in the vacuum chamber around the transmission line and Q is the gas throughput.

This experiment uses a Varian Turbo-V 250 turbo-molecular pump which has a pumping speed, in air, of $S_p = 250$ L s^{-1}. If we assume that the pressure drop between the pump inlet and the main vacuum chamber is negligible, then the throughput is $Q = S_p P_0$. For a chamber pressure of $P_0 = 0.25$ μTorr (which is typical for our experiment), $Q = 62.5$ μTorr · L/s.

For a finite tube with cross-sectional area A, the vacuum conductance for a gas with thermal velocity $\bar{v}$ is

$$C = \frac{1}{4}\bar{v}aA \tag{A.3}$$

where a is the transmission probability that a molecule will pass through the tube [35]. For the conductance channels in the input–output segment, $a = 0.51423$ [35]. If we use $\bar{v}$ for room-temperature air, then $C_{\text{ch}} = 0.485\ \text{L s}^{-1}$ and $C_{\text{io}} = 5.82\ \text{L s}^{-1}$. For an annular tube, like the quarter-wave transformers, the transmission probability can be obtained from

$$a = \left\{1 + \lambda\left[0.5 - \alpha\tan^{-1}(\lambda/\beta)\right]\right\}^{-1} \tag{A.4}$$

where

$$\alpha = \frac{0.0741 - 0.014\sigma - 0.037\sigma^2}{1 - 0.918\sigma + 0.050\sigma^2} \tag{A.5a}$$

$$\beta = \frac{5.825 - 2.86\sigma - 1.45\sigma^2}{1 + 0.56\sigma - 1.28\sigma^2} \tag{A.5b}$$

$$\lambda = \frac{l}{r_o - r_i} \tag{A.5c}$$

$$\sigma = \frac{r_i}{r_o} \tag{A.5d}$$

and l, r_i, and r_o are the tubes length and inner and outer radii, respectively [36]. Since the quarter-wave transformer is adjusted when we alter the gap between the inner and outer conductors, we now consider the worst-case configuration that occurs when fd $= 4.84$ GHz · mm. In this case, $a = 0.2407$ and the quarter-wave transformer's conductance is $C_{\text{QWT}} = 4.14\ \text{L s}^{-1}$. Combining this with C_{io} gives us a net conductance of $C_{\text{net}} = 4.83\ \text{L s}^{-1}$. Using these data and evaluating (A.2) gives us a pressure of $P_{\text{mp}} = 13.2\ \mu\text{Torr}$ in the multipacting region.

ACKNOWLEDGMENT

REFERENCES

[1] R. A. Kishek, Y. Y. Lau, L. K. Ang, A. Valfells, and R. M. Gilgenbach, "Multipactor discharge on metals and dielectrics: Historical review and recent theories," *Phys. Plasmas*, vol. 5, no. 5, pp. 2120–2126, May 1998.

[2] J. R. M. Vaughan, "Multipactor," *IEEE Trans. Electron Devices*, vol. ED-35, no. 7, pp. 1172–1180, Jul. 1988.

[3] R. Kishek and Y. Y. Lau, "Interaction of multipactor discharge and RF circuit," *Phys. Rev. Lett.*, vol. 75, no. 6, pp. 1218–1221, Aug. 1995.

[4] R. A. Kishek, "Interaction of multipactor discharge and RF structures," Ph.D. dissertation, Dept. Nuclear Eng. Radiological Sci., Univ. Michigan, Ann Arbor, MI, USA, 1997.

[5] P. Y. Wong, Y. Y. Lau, P. Zhang, N. Jordan, R. M. Gilgenbach, and J. Verboncoeur, "The effects of multipactor on the quality of a complex signal propagating in a transmission line," *Phys. Plasmas*, vol. 26, no. 11, Nov. 2019, Art. no. 112114.

[6] D. H. Preist and R. C. Talcott, "On the heating of output windows of microwave tubes by electron bombardment," *IRE Trans. Electron Devices*, vol. 8, no. 4, pp. 243–251, Jul. 1961.

[7] J. R. M. Vaughan, "Some high-power window failures," *IRE Trans. Electron Devices*, vol. 8, no. 4, pp. 302–308, Jul. 1961.

[8] M. Angelucci, A. Novelli, L. Spallino, A. Liedl, R. Larciprete, and R. Cimino, "Minimum thickness of carbon coating for multipacting suppression," *Phys. Rev. Res.*, vol. 2, no. 3, Aug. 2020, Art. no. 032030.

[9] A. J. Hatch, "Suppression of multipacting in particle accelerators," *Nucl. Instrum. Methods*, vol. 41, no. 2, pp. 261–271, May 1966.

[10] Y. Saito, S. Michizono, S. Anami, and S. Kobayashi, "Surface flashover on alumina RF windows for high-power use," *IEEE Trans. Electr. Insul.*, vol. 28, no. 4, pp. 566–573, Aug. 1993.

[11] D. Wu et al., "Fabrication of porous Ag/TiO₂/Au coatings with excellent multipactor suppression," *Sci. Rep.*, vol. 7, no. 1, p. 43749, Mar. 2017.

[12] E. A. H. Sleiman, J. Hillairet, M. Belhaj, and S. Dadouch, "Evaluation of multipactor thresholds for coaxial lines subject to surface conditioning for the WEST ion cyclotron antenna," *Fusion Eng. Design*, vol. 185, Dec. 2022, Art. no. 113325.

[13] I. Bojko, N. Hilleret, and C. Scheuerlein, "Influence of air exposures and thermal treatments on the secondary electron yield of copper," *J. Vac. Sci. Technol. A, Vac., Surf., Films*, vol. 18, no. 3, pp. 972–979, May 2000.

[14] T. P. Graves, "Experimental investigation of electron multipactor discharges at very high frequencies," Ph.D. dissertation, Massachusetts Inst. Technol., Cambridge, MA, USA, 2006.

[15] C. Chang, G. Z. Liu, C. X. Tang, C. H. Chen, H. Shao, and W. H. Huang, "Suppression of high-power microwave dielectric multipactor by resonant magnetic field," *Appl. Phys. Lett.*, vol. 96, no. 11, Mar. 2010, Art. no. 111502.

[16] R. L. Geng, H. Padamsee, S. Belomestnykh, P. Goudket, D. M. Dykes, and R. G. Carter, "Suppression of multipacting in rectangular coupler waveguides," *Nucl. Instrum. Methods Phys. Res. A, Accel. Spectrom. Detect. Assoc. Equip.*, vol. 508, no. 3, pp. 227–238, Aug. 2003.

[17] D. Gonzalez-Iglesias et al., "Multipactor in a coaxial line under the presence of an axial DC magnetic field," *IEEE Electron Device Lett.*, vol. 33, no. 5, pp. 727–729, May 2012.

[18] C. Jing et al., "Observation of multipactor suppression in a dielectric-loaded accelerating structure using an applied axial magnetic field," *Appl. Phys. Lett.*, vol. 103, no. 21, Nov. 2013, Art. no. 213503.

[19] X. Zhang, Y. Xiao, and B. Gimeno, "Multipactor suppression by a resonant static magnetic field on a dielectric surface," *IEEE Trans. Electron Devices*, vol. 67, no. 12, pp. 5723–5728, Dec. 2020.

[20] V. Semenov, A. Kryazhev, D. Anderson, and M. Lisak, "Multipactor suppression in amplitude modulated radio frequency fields," *Phys. Plasmas*, vol. 8, no. 11, pp. 5034–5039, Nov. 2001.

[21] D. González-Iglesias, O. Monerris, B. G. Martínez, M. E. Díaz, V. E. Boria, and P. M. Iglesias, "Multipactor RF breakdown in coaxial transmission lines with digitally modulated signals," *IEEE Trans. Electron Devices*, vol. 63, no. 10, pp. 4096–4103, Oct. 2016.

[22] D.-Q. Wen, A. Iqbal, P. Zhang, and J. P. Verboncoeur, "Suppression of single-surface multipactor discharges due to non-sinusoidal transverse electric field," *Phys. Plasmas*, vol. 26, no. 9, Sep. 2019, Art. no. 093503.

[23] Y. Huo, W. Liu, C. Ke, C. Chang, and C. Chen, "Sharp improvement of flashover strength from composite micro-textured surfaces," *J. Appl. Phys.*, vol. 122, no. 11, Sep. 2017, Art. no. 115105.

[24] M. Pivi, F. K. King, R. E. Kirby, T. O. Raubenheimer, G. Stupakov, and F. Le Pimpec, "Sharp reduction of the secondary electron emission yield from grooved surfaces," *J. Appl. Phys.*, vol. 104, no. 10, Nov. 2008, Art. no. 104904.

[25] D. Wright, Z. C. Shaw, J. J. Mankowski, J. C. Dickens, J. Stephens, and A. A. Neuber, "Multipactor suppression via asymmetric grooves in S-band waveguide," *Phys. Plasmas*, vol. 29, no. 6, Jun. 2022, Art. no. 063108.

[26] M. Ye et al., "Suppression of secondary electron yield by microporous array structure," *J. Appl. Phys.*, vol. 113, no. 7, Feb. 2013, Art. no. 074904.

[27] E. D. Weber, M. Mirmozafari, N. Behdad, and J. H. Booske, "Experimental verification of multipactor suppression in microstripline using high porosity surfaces," *IEEE Trans. Plasma Sci.*, vol. 50, no. 1, pp. 43–49, Jan. 2022.

[28] *The Evolution of an Idea: A Brief Typology of 3D Printing*. Cambridge, MA, USA: MIT Press, 2019.

[29] *Copper Material Datasheet, Rev. 1.1*, Markforged, Waltham, MA, USA, Jan. 2022.

[30] S. V. Langellotti, "Multipactor in coaxial transmission lines," Ph.D. dissertation, Dept. Nuclear Eng. Radiological Sci., Univ. Michigan, Ann Arbor, MI, USA, 2022.

[31] S. V. Langellotti, N. M. Jordan, Y. Y. Lau, and R. M. Gilgenbach, "Multipactor experiments on an S-band coaxial test cell," *Rev. Sci. Instrum.*, vol. 92, no. 12, Dec. 2021, Art. no. 124706.

[32] C. Vicente, M. Mattes, D. Wolk, H. L. Hartnagel, J. R. Mosig, and D. Raboso, "Contribution to the RF breakdown in microwave devices and its prediction," in *Proc. 27th Int. Power Modulator Symp.*, May 2006, pp. 22–27.

[33] R. A. Kishek, "Ping-pong modes: A new form of multipactor," *Phys. Rev. Lett.*, vol. 108, no. 3, Jan. 2012, Art. no. 035003.

[34] R. A. Kishek, "Ping-pong modes and higher-periodicity multipactor," *Phys. Plasmas*, vol. 20, no. 5, May 2013, Art. no. 056702.

[35] J. F. O'Hanlon, *A User's Guide to Vacuum Technology*, 3rd ed. Hoboken, NJ, USA: Wiley-Interscience, 2003.

[36] A. S. Berman, "Free molecule flow in an annulus," *J. Appl. Phys.*, vol. 40, no. 12, pp. 4991–4992, Nov. 1969.